

Origin of switchable quasiparticle-interference chirality in loop-current phase of kagome metals measured by scanning-tunneling-microscopy

Seigo Nakazawa¹, Rina Tazai², Youichi Yamakawa¹, Seiichiro Onari¹, and Hiroshi Kontani¹

¹*Department of Physics, Nagoya University, Furo-cho, Nagoya 464-8602, Japan*

²*Yukawa Institute for Theoretical Physics, Kyoto University, Kyoto 606-8502, Japan.*

(Dated: March 11, 2025)

The chiral loop-current (LC) phase in kagome metals AV_3Sb_5 ($A = \text{Cs, Rb, K}$) has attracted considerable attention as a novel quantum state driven by electron correlations. Scanning tunneling microscopy (STM) experiments have provided strong evidence for the chiral LC phase through the detection of chirality in the quasiparticle interference (QPI) signal. However, the fundamental relationship between “QPI chirality” and “LC chirality” remains unexplored. For instance, the QPI signal is unchanged even when all LC orders are inverted. Furthermore, only the chiral LC order cannot induce QPI chirality. At present, the true essence of kagome metals that we should learn from the remarkable QPI experiments remains elusive. To address this, we investigate the origin of the QPI signal in the LC phase using a large unit-cell tight-binding model for kagome metals. The LC phase gives rise to a Z_3 nematic phase, characterized by three distinct directors, under the Star-of-David bond order. Our findings demonstrate that the QPI chirality induced by a single impurity at site Z , denoted as χ_Z , can take values of ± 1 (chiral) or 0 (achiral), depending on the direction of the Z_3 nematic order. Prominent QPI chirality originates from extremely dilute impurities ($\lesssim 0.1\%$) in the present mechanism. Notably, χ_Z ($= \pm 1, 0$) changes smoothly with minimal free-energy barriers by applying a small magnetic field B_z , accompanied by a switching of the Z_3 nematic director. This study provides a comprehensive explanation for the observed “ B_z -switchable QPI chirality” in regions with dilute impurities, offering fundamental insight into the chiral LC in kagome metals.

Introduction

In strongly correlated metals, a variety of quantum phase transitions have been discovered over the years, leading to intriguing electronic states due to the breaking of symmetries like time-reversal symmetry (TRS), rotational symmetry, and chirality. The recently discovered kagome metal AV_3Sb_5 ($A = \text{Cs, Rb, K}$) [1, 2] displays remarkable electronic states arising from a sequence of quantum phases, including charge density wave (CDW) [3–5], nematic states [3, 6–9], and superconductivity [10, 11]. Particularly, the TRS-breaking loop-current (LC) state, which lacks spin polarization, has garnered significant attention [12–16]. The LC order parameter involves a “pure imaginary” modulation in the hopping integral, $\delta t^c = \pm i\eta$ [9, 17–25].

The kagome lattice structure and the Fermi surfaces without density waves are shown in Figure 1 (a). Figure 1 (b) depicts the “chiral LC” state that violates any 2D mirror symmetries, characterized by $\delta t^c \neq 0$ in all ab-, bc-, and ca-directions [9, 19–25]. This state is associated with a finite uniform orbital magnetization (M_{orb}), which can be switched by a small out-of-plane magnetic field B_z , as evidenced by the anomalous Hall effect (AHE) [26–28] and electronic magneto-chiral anisotropy (eMChA) [29]. The CDW order parameter, $\delta t^b = \pm\phi$ (real), is also illustrated in Fig. 1 (b) [9]; see Supplementary Information (SI) A for details [30]. The microscopic mechanism of the LC order has been investigated in Refs. [9, 19–25], including the BO fluctuation-mediated mechanism [31].

Experimentally, the TRS breaking electronic states in the chiral LC phase have been reported by scanning tun-

neling microscopy (STM) [12–16], μSR [32–35], NMR [36], Kerr effect [7, 37], and AHE [26–28] measurements. Notably, nonreciprocal transport measurement by eMChA [29] reveals the violations of both TRS and inversion symmetries. Many of these experiments indicate the chiral LC appears at $\sim T_{\text{lc}}$ inside the CDW phase ($T < T_{\text{cdw}} \sim 100\text{K}$). Recent study [38] shows that T_{lc} drastically increases under the weak magnetic field B_z or tiny strain ϵ , which is naturally explained based on the extended Ginzburg-Landau free-energy theory [39]. Additionally, magnetic torque measurements [8] suggest that an achiral LC without M_{orb} appears around $\sim 130\text{K}$. Theoretically, achiral to chiral LC transition is triggered by the uniform magnetic field or the CDW order parameter below T_{cdw} .

Intuitive and strong evidence of the chiral LC order below T_{cdw} comes from the STM measurements, which reveal chirality in the quasiparticle interference (QPI) signal induced by dilute impurities. The QPI signal is the Fourier transform of the local density of states (LDOS) over a large area, including 1,000 – 10,000 sites. (QPI experiments can reveal fundamental quantum orders in metals, including the nematic/smectic density-wave states [40, 41] and the pair-density-wave states [42].) Notably, the observed chirality in the QPI signal in the LC phase is switched by small B_z in $A=\text{K}$ [12, 13], $A=\text{Cs}$ [13, 15], and $A=\text{Rb}$ [14, 16] compounds. However, the fundamental relationship between QPI chirality and LC chirality remains unexplored. For instance, the QPI signal remains unchanged even when all LC orders are inverted (by B_z), because the LDOS is TRS-even (*i.e.*, η -even) and thus unaffected. Furthermore, the presence

of only the chiral LC order cannot induce QPI chirality, despite the induction of a finite M_{orb} . Consequently, despite the significance of QPI experiments in kagome metals [12–16], the underlying origin of QPI chirality remains poorly understood.

To address this unresolved issue, in this paper, we investigate the origin of the QPI signal in the LC phase using a large unit-cell model for kagome metals. The coexistence of LC and BO gives rise to the three-directional (Z_3) nematic phase. Our findings show that the QPI chirality due to the single impurity at site Z, denoted as χ_Z , takes ± 1 (chiral) or 0 (achiral), depending on the director of the Z_3 LC + BO nematic order. Importantly, prominent QPI chirality originates from extremely dilute impurities ($\lesssim 0.1\%$). Remarkably, χ_Z changes by applying a small magnetic field B_z , accompanied by a change of Z_3 nematic director with minimal free-energy barriers. This study provides a highly promising explanation for the B_z -reversible QPI chirality observed in regions with dilute impurities, offering essential insight into the chiral LC phase in kagome metals.

The microscopic mechanism of the exotic multiple quantum phase transitions has been studied very actively. The mean-field theories as well as the renormalization group theories based on the (extended) Hubbard models have been performed in Refs. [9, 19, 23, 24, 31, 43–45]. We discovered that the Star-of-David (SoD) BO state is driven by the “paramagnon-interference” mechanism [9], which is described by the Aslamazov-Larkin vertex corrections that are dropped in the mean-field level approximations [46–50]. Importantly, the BO fluctuations mediate not only s -wave or p -wave superconductivity but also the TRS breaking LC order [9, 31].

Kagome lattice model with LC + BO orders

First, we introduce the kagome lattice model [9, 43] shown in Fig. 1 (a). The original unit cell is composed of three sublattices a, b, and c. We put the nearest and the next-neighbor hopping integrals, $t = -0.5$ eV and $t' = -0.04$ eV, to approximate the real Fermi surface and set the temperature $T = 0.0025$ eV. Hereafter, the unit of energy is eV. Fermi surfaces without density waves are also shown. Here, red, blue, and green colors denote the weight of the sublattices a, b, and c, respectively. Figure 1 (b) shows the enlarged 12 site unit cell under the triple- \mathbf{q} order. We introduce the LC order $\boldsymbol{\eta} \equiv (\eta_1, \eta_2, \eta_3)$ and the BO $\boldsymbol{\phi} \equiv (\phi_1, \phi_2, \phi_3)$, where η_n and ϕ_n are the order parameters with the wavevector \mathbf{q}_n . The definitions of the LC $\boldsymbol{\eta}$ and the BO $\boldsymbol{\phi}$ are given in the SI A.

When $T_{\text{cdw}} > T_{\text{lc}}$, we can set the BO as $\boldsymbol{\phi}_0 = \phi_0 \mathbf{e}_0$ without the loss of generality, where $\mathbf{e}_0 = (1, 1, 1)/\sqrt{3}$. Then, just below T_{lc} , the LC order that minimize the GL free energy is given as $\boldsymbol{\eta}_\alpha = \eta_\alpha \mathbf{e}_\alpha$ ($\alpha = \text{I, II, III}$), where $\mathbf{e}_{\text{I}} = (2, -1, -1)/\sqrt{6}$, $\mathbf{e}_{\text{II}} = (-1, 2, -1)/\sqrt{6}$, and $\mathbf{e}_{\text{III}} =$

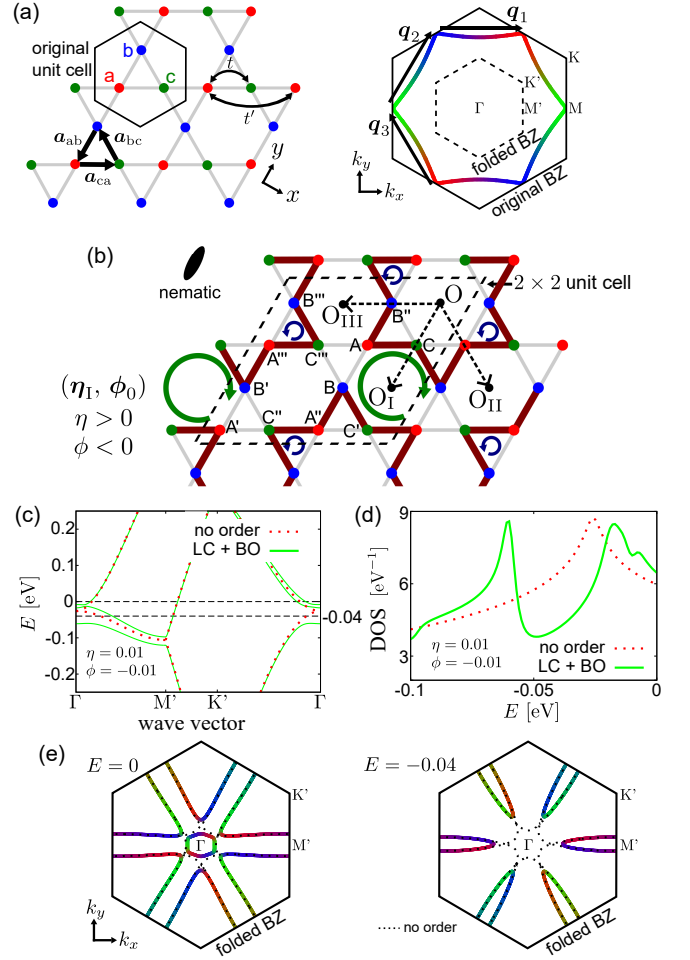


FIG. 1: (a) Kagome lattice model. The unit cell is composed of the sublattices a, b, and c. $2\mathbf{a}_{ab}$, $2\mathbf{a}_{bc}$ give the two primitive vectors. Fermi surfaces without density waves are also shown. Red, blue, and green colors represent the weight of the sublattices a, b, and c, respectively. (b) Nematic LC + BO existing state with $\boldsymbol{\phi}_0$ and $\boldsymbol{\eta}_{\text{I}}$. The director is along y (or equivalently x) axis. The 2×2 unit cell is composed of 12 sites Z, Z', Z'', and Z''' with Z = A, B, C. The C_6 center of $\boldsymbol{\eta}_\alpha$ is denoted as O_α . (c) Band structure and (d) DOS in the folded BZ for $-\phi = \eta = 0.01$. (e) Equal-energy surface for $E = 0$ (Fermi level) and $E = -0.04$.

$(-1, -1, 2)/\sqrt{6}$. Figure 1 (b) shows the SoD BO by $\boldsymbol{\phi}_0$ ($\phi < 0$) and the LC order by $\boldsymbol{\eta}_{\text{I}}$ ($\eta > 0$): The band structure and the density-of-states (DOS) are shown in Figs. 1 (c) and (d) in the folded Brillouin zone (BZ) for $\eta = -\phi = 0.01$. The equal-energy surfaces for $E = 0$ (Fermi level) and -0.04 are shown in Fig. 1 (e).

Importantly, the coexisting state $(\boldsymbol{\eta}_\alpha, \boldsymbol{\phi}_0)$ is nematic because the C_6 symmetry center of the LC, O_α , and that of the BO, O , are different. The director is along $O-O_\alpha$ line; See the SI A for details [30]. In the LC + BO state in kagome metals, dilute impurities cause nontrivial sizable change in the electronic states [51]. To reveal the origin of the impurity-induced chiral QPI signal in kagome metals,

we investigate the single impurity effect based on the giant unit-cell kagome lattice model ($N \sim 1500$):

$$H = \sum_{\mathbf{k}} \sum_{i,j,\sigma} t_{\mathbf{k},i,j} c_{\mathbf{k},i,\sigma}^\dagger c_{\mathbf{k},j,\sigma} + V \sum_{\sigma} c_{\mathbf{k},Z,\sigma}^\dagger c_{\mathbf{k},Z,\sigma}, \quad (1)$$

where i, j ($= 0 \sim N - 1$) represents the site indices in the unit-cell, and V is the impurity potential at site Z . Hereafter, we set $V = \infty$. \mathbf{k} is the wavevector due to the periodic configuration of the giant unit-cell. The hopping integral is $t_{\mathbf{k},i,j} = t_{\mathbf{k},i,j}^0 + \delta t_{\mathbf{k},i,j}^c + \delta t_{\mathbf{k},i,j}^b$, where $t_{\mathbf{k},i,j}^0$ is the original hopping integral with D_{6h} symmetry, $\delta t_{\mathbf{k},i,j}^c$ and $\delta t_{\mathbf{k},i,j}^b$ are the LC and BO parameters; see the SI A [30]. The LDOS at site i is $\rho_i(E) = \frac{1}{N} \sum_{\mathbf{k}} \delta(\epsilon_{b,\mathbf{k}} - E) |U_{i,b}(\mathbf{k})|^2$, where $b = 1 \sim N$ is the band index. Here, $\epsilon_{b,\mathbf{k}}$ is the Bloch band-energy measured from the chemical potential, and $U_{i,b}(\mathbf{k})$ is the matrix element of the unitary transformation from i to b . We use $\geq 2048^2$ \mathbf{k} -meshes in the numerical study.

QPI signal chirality

Figure 2 (a) represents the modulation of the LDOS ($\delta\rho_i \equiv \rho_i - \rho_i^{V=0}$) at $E = -0.04$ induced by the single impurity at A-site (=Imp A), whose location is shown in Fig. 1 (b). We set $N = 12M_xM_y$ -site unit cell with $M_x = M_y = 11$ ($N = 1452$) under the LC + BO state with $-\phi = \eta = 0.01$. (The QPI measurements in Refs. [12–16] were performed for $N = 5000 \sim 10000$ V sites.) Thus, a single impurity induces long-range modulation in $\rho_i(E)$, driven by significant Friedel oscillations in the LC + BO phase [51]. The present LDOS pattern is achiral because any 2D mirror symmetries are violated. This fact leads to the chiral QPI signal, as we will discuss in the paper. (The LDOS pattern without LC exhibit mirror symmetry; see the SI A [30].) The symmetry of the obtained LDOS pattern governs the QPI signals, which is given by the Fourier transformation of the LDOS:

$$I_{\mathbf{q}}(E) = \left| \sum_i \rho_i(E) e^{i\mathbf{q}\cdot\mathbf{r}_i} \right| = \left[\sum_{i,j} \rho_i(E) \rho_j(E) \cos(\mathbf{q}\cdot(\mathbf{r}_i - \mathbf{r}_j)) \right]^{\frac{1}{2}}. \quad (2)$$

Without impurities, the QPI signal exhibits sharp Bragg peaks at $\mathbf{q} = 2\mathbf{q}_n$ and $\mathbf{q} = \mathbf{q}_n$, as shown in Fig. 2 (b). The former (latter) originates from the 3-site (the 12-site) unit-cell. The QPI signal exhibits the nematic (achiral) peak structure; $I_1 \neq I_2 = I_3$ ($I_n \equiv I_{\mathbf{q}_n}$). Notably, a single impurity causes a dramatic change in the QPI signal in the large site model, as shown in Fig. 2 (c). Figure 2 (d) exhibits the E -dependence of the QPI signal due to Imp A for $N = 1452$ model. Importantly, the QPI signal exhibits the chiral peak structure; $I_1 \neq I_2 \neq I_3$. Here, we

define the QPI chirality due to Imp A as $\chi_A \equiv \varepsilon_{n_1 n_2 n_3}$ for $I_{n_1} > I_{n_2} > I_{n_3}$. (ε_{nml} is a Levi-Civita tensor.) Interestingly, χ_A depends on the energy E . These results are consistent with experimental reports [12–16]. Thus, the chiral QPI signal in kagome metals is naturally explained by the LC + BO nematic state predicted in Ref. [31]. This is the main finding of this study.

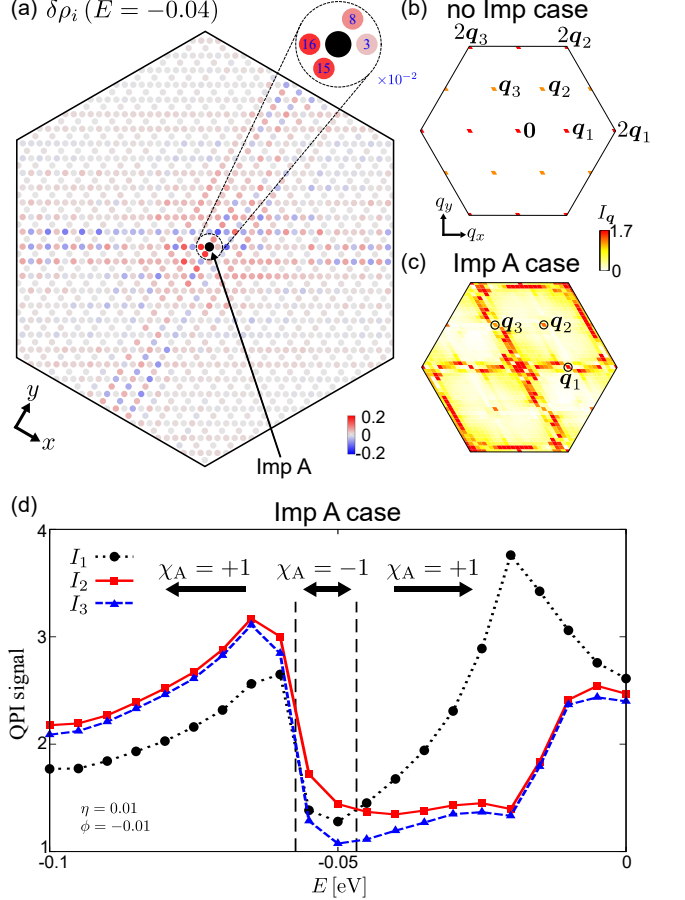


FIG. 2: (a) Modulation of the LDOS $\delta\rho_i$ ($E = -0.04$) induced by Imp A in $N = 1452$ -site unit cell under the LC + BO state with (η_1, ϕ_0) . Single impurity gives drastic long-range modulation, reflecting the chirality of the LC phase. (Inset) LDOS of the four sites around Imp A. (b) QPI signals $I_{\mathbf{q}}$ for $V = 0$. $2\mathbf{q}_n$ is the Bragg peak of the 3-site unit-cell, and \mathbf{q}_n is the Bragg peak of the 12-site due to LC + BO order. (c) QPI signals for $V = \infty$ given by the Fourier transformation of the LDOS shown in (a). (d) E -dependence of the QPI signal (I_1, I_2, I_3) due to a single Imp A, whose chirality is defined as $\chi_A \equiv \varepsilon_{n_1 n_2 n_3}$ for $I_{n_1} > I_{n_2} > I_{n_3}$.

Here, we discuss the origin of the QPI chirality from the perspective of symmetry. Figure 3 (a) [(b)] shows the LDOS in the LC [BO] state at $E = -0.05$ for $V = 0$. In both LC and BO states, C_6 symmetry is preserved for around O_1 and O , respectively. Because $O_1 \neq O$, the symmetry of the LDOS in the LC + BO state shown in Fig. 3 (c) is reduced to C_2 , while two mirror symmetries M_x ($x \rightarrow -x$) and M_y ($y \rightarrow -y$) survive. Thus, the

LDOS for $V = 0$ exhibits four different values. Now, we discuss the chiral symmetry induced by a single impurity. For Imp A state, all in-plane mirror symmetries are broken, and it transforms into the Imp B state by M_y operation for (η_I, ϕ_0) . Therefore, if $\chi_A = -1$ for Imp A state, then $\chi_B = +1$ for Imp B state. In contrast, the Imp C state is unchanged by M_x operation, so the electronic state is achiral $\chi_C = 0$. The numerically derived QPI signals for Imp A-C states are depicted in Fig. 3 (d). Thus, when the director of the LC + BO nematicity is along ab direction, the QPI chirality emerges for Imp A and Imp B states, and the relation $\chi_A = -\chi_B$ holds. It is noteworthy that the chiral QPI signal appears when two impurities are introduced in sites A and A', where the inversion-symmetry holds. Therefore, the chiral QPI originates from the 2D mirror symmetry violations, even if 2D inversion symmetry ($I = M_x M_y$) holds.

Change of χ_Z by magnetic field

Now, we explain that the QPI chirality by Imp Z ($\chi_Z = \pm 1, 0$) is changed by small magnetic field along z -axis, B_z . As we explain in the SI B [30], the GL free energy for (η, ϕ_0) is given as $F[\eta, \phi_0] = A_c |\eta|^2 + B(\eta_1 + \eta_2 + \eta_3)^2 + C|\eta|^4 + C'(\eta_1^2 \eta_2^2 + \text{cycl.})$, where $\eta_0 \equiv |\eta|$ and A_c, B, C and C' are the GL coefficients renormalized by ϕ . We assume ϕ is independent of η , which is justified when $|\eta| \ll |\phi|$ for $T_{\text{cdw}} \gg T_{\text{lc}} \gtrsim T$. In addition, we can expect the relation $C' \ll C$ and $B > 0$ in kagome metals. Then, $F[\eta, \phi_0]$ is minimized when (i) $|\eta| \equiv \eta_0$ (= const.) and (ii) $\eta_1 + \eta_2 + \eta_3 = 0$.

As we explain in the SI B [30], the orbital magnetization is $M_{\text{orb}} = m_3 \eta_1 \eta_2 \eta_3$ under the constraint (ii). Therefore, in the case of $m_3 < 0$, the state η_α is realized under $B_z > 0$, and it is changed to $-\eta_{\alpha'}$ under $B_z < 0$. Now, we consider the adiabatic change from η_I to $-\eta_\alpha$ under the constraints (i) and (ii). Figure 4 (a) illustrates the process $\eta_I \rightarrow -\eta_{III}$ as a function of η_2 . This process occurs under B_z because M_{orb} undergoes a monotonic change with a sign reversal. Importantly, by applying a $+\pi/3$ rotation around the BO center O , the state $(-\eta_{III}, \phi_0)$ transforms into $(-\eta_I, \phi_0)$, exhibiting the same LDOS pattern shown in Fig. 3 (c). Since the same rotation maps Imp A to Imp B', it follows that $\chi_A(-\eta_{III}, \phi_0)$ is equal to $\chi_{B'}(-\eta_I, \phi_0) = +1$. (Note that both the LDOS and the QPI signal remain invariant under the transformation $\eta \rightarrow -\eta$.) Similarly, the transition from η_I to $-\eta_{II}$ can also be realized, leading to $\chi_A(-\eta_{II}, \phi_0) = \chi_{C''}(-\eta_I, \phi_0) = 0$. In contrast, the process $\eta_I \rightarrow -\eta_I$ shown in Fig. 4 (b) would be difficult to be realized under B_z because M_{orb} exhibits non-monotonic behavior. In summary, the QPI chirality $\chi_Z = 0, \pm 1$ changes by applying tiny B_z . This theory provides a consistent explanation for the switchable chiral QPI signal in kagome metals.

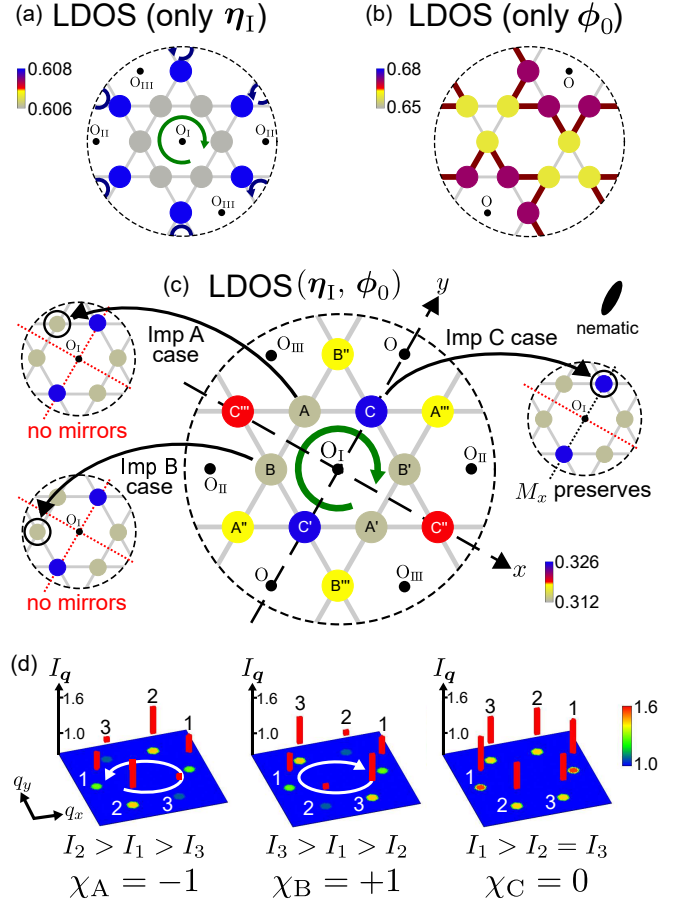


FIG. 3: (a) LDOS under the LC order $(\eta, \phi) = (0.01, 0)$ and (b) LDOS under the BO order $(\eta, \phi) = (0, -0.01)$ for $V = 0$ at $E = -0.05$. Both states have C_6 symmetry. (c) LDOS under the LC + BO order [$\eta = -\phi = 0.01$] with C_2 symmetry. All mirror symmetries are violated by a single impurity at A-site or B-site. Therefore, the chirality is induced by a single impurity. In contrast, a mirror symmetries survive by the C-site impurity. (d) Obtained QPI signal at $E = -0.05$, which is chiral for A-site impurity ($\chi_A = -1$) and B-site impurity ($\chi_B = +1$), while it is achiral for C-site impurity ($\chi_C = 0$).

The QPI signals due to Imp Z and Imp Z' (Z=A, B, C) shown in Fig. 3 (c) are equivalent. However, the QPI signals due to Imp Z'' (Imp Z''') are different from those due to Imp Z, from the perspective of symmetry. In the SI C [30], we show that the magnitude of the QPI signal chirality is very small for Imp Z'' case.

Discussions

Experimentally, the QPI signal becomes chiral in the dilute impurity region. When $n_{\text{imp}} \approx 0.1\%$ in $N \approx 5000$ site model, a single impurity is likely to occupy an A, A', B, or B' site in Fig. 3 (c), giving rise to the chiral QPI signal. Furthermore, the Sb-site impurity (or vacancy) also induces sizable chiral QPI, as we discuss in

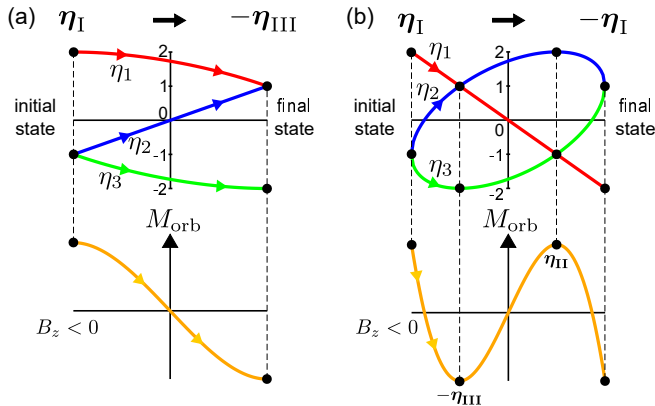


FIG. 4: (a) Adiabatic change from η_I to $-\eta_{III}$ under the constant $|\eta| = \eta_0 = \sqrt{6}$ and $\eta_I + \eta_2 + \eta_3 = 0$. The corresponding $M_{\text{orb}} \propto \eta_1 \eta_2 \eta_3$ exhibits a monotonic change. Therefore, the transition from η_I to $-\eta_{III}$ (or $-\eta_{II}$) can be induced by the outer magnetic field B_z . (b) Adiabatic change from η_I to $-\eta_I$ under the constant $|\eta|$. Because $M_{\text{orb}} \propto \eta_1 \eta_2 \eta_3$ is non-monotonic, the transition from η_I to $-\eta_I$ is not realized.

the SI D [30]. Note that the QPI signal becomes nematic for impurity-free region for $A=K$ [3, 13]. These observations are consistently explained by the present theory. Notably, in the dense impurity region, the QPI signal transitions to a nematic state, possibly due to the suppression of the LC order [51].

In Table I, we summarize the sign of M_{orb} , the direction of the nematicity, and the sign of the Imp-Z induced QPI chirality χ_Z in the Z_3 nematic LC + BO Z_3 state ($\pm\eta_\alpha, \phi_0$). Here, $Z = A, B, \text{ or } C$, and $\alpha = I, II, \text{ or } III$. In this Table, we define the sign of M_{orb} and χ_A is + for the LC + BO state (η_I, ϕ_0).

TABLE I: M_{orb} , director, and Imp-Z induced QPI chirality χ_Z in the Z_3 nematic LC + BO state ($\pm\eta_\alpha, \phi_0$).

LC	η_I	η_{II}	η_{III}	$-\eta_I$	$-\eta_{II}$	$-\eta_{III}$
M_{orb}	+	+	+	-	-	-
director	0	$\pi/3$	$2\pi/3$	0	$\pi/3$	$2\pi/3$
χ_A	+	0	-	+	0	-
χ_B	-	+	0	-	+	0
χ_C	0	-	+	0	-	+

Here, we explore the possibility of impurity-free chiral QPI for $A = \text{Cs}$ and Rb , where $2a_0$ and $4a_0$ stripe CDW is commonly observed in STM studies [52, 53]. (Note that this stripe order is absent for $A = K$.) As discussed in Ref. [54], the stripe CDW breaks inversion symmetry when it coexists with the LC order. If the Z_3 nematic director is not aligned with the stripe CDW, a chiral QPI signal ($I_1 \neq I_2 \neq I_3$) emerges even in the absence of impurities, as explained in SI E [30].

The 3Q-LC state exhibits weak bulk ferromagnetism ($M_{\text{orb}} \neq 0$) when the wavevectors \mathbf{q}_n ($n = 1, 2, 3$) are

commensurate. However, domains with opposite signs of M_{orb} may form if \mathbf{q}_n are slightly incommensurate. In such cases, applying a small B_z field would restore bulk ferromagnetism to gain the Zeeman energy.

In summary, we present the switchable chiral QPI signal in kagome metals as decisive evidence for the emergence of LC order in the BO phase. Prominent QPI chirality originates from extremely dilute impurities ($\lesssim 0.1\%$) in kagome metals. Interestingly, the chirality of the QPI is found to be strongly correlated with the Z_3 nematicity originating from the off-site LC + BO state [31]. Furthermore, this study represents an important step toward understanding the chirality in the pair-density-wave state recently reported in kagome metals [13]. In this study, we have omitted the m-type Fermi surface, formed by d_{yz} orbitals, which is quantitatively important for the LC-induced M_{orb} [39] and eMChA [54]. Therefore, the influence of the m-type Fermi surface on the chiral QPI signal will be an important future issue.

Acknowledgments

We are grateful to Y. Matsuda, T. Shibauchi, K. Hashimoto, T. Asaba, and S. Suetsugu for very useful discussions.

-
- [1] B. R. Ortiz, L. C. Gomes, J. R. Morey, M. Winiarski, M. Bordelon, J. S. Mangum, I. W. H. Oswald, J. A. Rodriguez-Rivera, J. R. Neilson, S. D. Wilson, E. Ertekin, T. M. McQueen, and E. S. Toberer, New kagome prototype materials: discovery of KV_3Sb_5 , RbV_3Sb_5 , and CsV_3Sb_5 , *Phys. Rev. Materials* **3**, 094407 (2019).
 - [2] B. R. Ortiz, S. M. L. Teicher, Y. Hu, J. L. Zuo, P. M. Sarte, E. C. Schueller, A. M. M. Abeykoon, M. J. Krogstad, S. Rosenkranz, R. Osborn, R. Seshadri, L. Balents, J. He, and S. D. Wilson, CsV_3Sb_5 : A \mathbb{Z}_2 Topological kagome metal with a superconducting ground state, *Phys. Rev. Lett.* **125**, 247002 (2020).
 - [3] H. Li, H. Zhao, B. R. Ortiz, T. Park, M. Ye, L. Balents, Z. Wang, S. D. Wilson, and I. Zeljkovic, Rotation symmetry breaking in the normal state of a kagome superconductor KV_3Sb_5 , *Nat. Phys.* **18**, 265 (2022).
 - [4] L. Nie, K. Sun, W. Ma, D. Song, L. Zheng, Z. Liang, P. Wu, F. Yu, J. Li, M. Shan, D. Zhao, S. Li, B. Kang, Z. Wu, Y. Zhou, K. Liu, Z. Xiang, J. Ying, Z. Wang, T. Wu, and X. Chen, Charge-density-wave-driven electronic nematicity in a kagome superconductor, *Nature* **604**, 59 (2022).
 - [5] T. Kato, Y. Li, T. Kawakami, M. Liu, K. Nakayama, Z. Wang, A. Moriya, K. Tanaka, T. Takahashi, Y. Yao, and T. Sato, Three-dimensional energy gap and origin of charge-density wave in kagome superconductor KV_3Sb_5 , *Commun. Mater.* **3**, 30 (2022).
 - [6] L. Nie, K. Sun, W. Ma, D. Song, L. Zheng, Z. Liang, P. Wu, F. Yu, J. Li, M. Shan, D. Zhao, S. Li, B. Kang, Z. Wu, Y. Zhou, K. Liu, Z. Xiang, J. Ying, Z. Wang, T.

- Wu, and X. Chen, Charge-density-wave-driven electronic nematicity in a kagome superconductor, *Nature* **604**, 59 (2022).
- [7] Y. Xu, Z. Ni, Y. Liu, B. R. Ortiz, Q. Deng, S. D. Wilson, B. Yan, L. Balents, and L. Wu, Three-state nematicity and magneto-optical Kerr effect in the charge density waves in kagome superconductors, *Nat. Phys.* **18**, 1470 (2022).
- [8] T. Asaba, A. Onishi, Y. Kageyama, T. Kiyosue, K. Ohtsuka, S. Suetsugu, Y. Kohsaka, T. Gaggli, Y. Kasahara, H. Murayama, K. Hashimoto, R. Tazai, H. Kontani, B. R. Ortiz, S. D. Wilson, Q. Li, H.-H. Wen, T. Shibauchi, and Y. Matsuda, Evidence for an odd-parity nematic phase above the charge-density-wave transition in a kagome metal, *Nat. Phys.* **20**, 40 (2024).
- [9] R. Tazai, Y. Yamakawa, S. Onari, and H. Kontani, Mechanism of exotic density-wave and beyond-Migdal unconventional superconductivity in kagome metal AV_3Sb_5 ($A=K, Rb, Cs$), *Sci. Adv.* **8**, eabl4108 (2022).
- [10] M. Roppongi, K. Ishihara, Y. Tanaka, K. Ogawa, K. Okada, S. Liu, K. Mukasa, Y. Mizukami, Y. Uwatoko, R. Grasset, M. Konczykowski, B. R. Ortiz, S. D. Wilson, K. Hashimoto, and T. Shibauchi, Bulk evidence of anisotropic s -wave pairing with no sign change in the kagome superconductor CsV_3Sb_5 , *Nat Commun* **14**, 667 (2023).
- [11] W. Zhang, X. Liu, L. Wang, C. W. Tsang, Z. Wang, S. T. Lam, W. Wang, J. Xie, X. Zhou, Y. Zhao, S. Wang, J. Tallon, K. T. Lai, and S. K. Goh, Nodeless superconductivity in kagome metal CsV_3Sb_5 with and without time reversal symmetry breaking, *Nano Lett.* **23**, 872 (2023).
- [12] Y.-X. Jiang, J.-X. Yin, M. M. Denner, N. Shumiya, B. R. Ortiz, G. Xu, Z. Guguchia, J. He, M. S. Hossain, X. Liu, J. Ruff, L. Kautzsch, S. S. Zhang, G. Chang, I. Belopolski, Q. Zhang, T. A. Cochran, D. Multer, M. Litskevich, Z.-J. Cheng, X. P. Yang, Z. Wang, R. Thomale, T. Neupert, S. D. Wilson, and M. Z. Hasan, Unconventional chiral charge order in kagome superconductor KV_3Sb_5 , *Nat. Mater.* **20**, 1353 (2021).
- [13] H. Deng *et al.*, Chiral kagome superconductivity modulations with residual Fermi arcs, *Nature* **632**, 775 (2024).
- [14] Y. Xing, S. Bae, E. Ritz, Fan Yang, Turan Birol, Andrea N. Capa Salinas, Brenden R. Ortiz, Stephen D. Wilson, Z. Wang, R. M. Fernandes, and V. Madhavan, *Nature* **631**, 60 (2024).
- [15] Z. Wang *et al.*, Electronic nature of chiral charge order in the kagome superconductor CsV_3Sb_5 , *Phys. Rev. B* **104**, 075148 (2021).
- [16] N. Shumiya *et al.*, Intrinsic nature of chiral charge order in the kagome superconductor RbV_3Sb_5 , *Phys. Rev. B* **104**, 035131 (2021).
- [17] C. M. Varma, Non-Fermi-liquid states and pairing instability of a general model of copper oxide metals, *Phys. Rev. B* **55**, 14554 (1997).
- [18] C. Weber, T. Giamarchi, and C. M. Varma, *Phase Diagram of a Three-Orbital Model for High- T_c Cuprate Superconductors*, *Phys. Rev. Lett.* **112**, 117001 (2014).
- [19] T. Park, M. Ye, and L. Balents, Electronic instabilities of kagome metals: Saddle points and Landau theory, *Phys. Rev. B* **104**, 035142 (2021).
- [20] Y.-P. Lin and R. M. Nandkishore, Complex charge density waves at Van Hove singularity on hexagonal lattices: Haldane-model phase diagram and potential realization in the kagome metals AV_3Sb_5 ($A=K, Rb, Cs$), *Phys. Rev. B* **104**, 045122 (2021).
- [21] M. L. Kiesel, C. Platt, and R. Thomale, Unconventional Fermi surface instabilities in the kagome Hubbard model, *Phys. Rev. Lett.* **110**, 126405 (2013).
- [22] W.-S. Wang, Z.-Z. Li, Y.-Y. Xiang, and Q.-H. Wang, Competing electronic orders on kagome lattices at van Hove filling, *Phys. Rev. B* **87**, 115135 (2013).
- [23] X. Wu, T. Schwemmer, T. Müller, A. Consiglio, G. Sangiovanni, D. D. Sante, Y. Iqbal, W. Hanke, A. P. Schnyder, M. M. Denner, M. H. Fischer, T. Neupert, and R. Thomale, Nature of Unconventional Pairing in the Kagome Superconductors AV_3Sb_5 ($A = K, Rb, Cs$), *Phys. Rev. Lett.* **127**, 177001 (2021).
- [24] M. M. Denner, R. Thomale, and T. Neupert, Analysis of Charge Order in the Kagome Metal AV_3Sb_5 ($A = K, Rb, Cs$), *Phys. Rev. Lett.* **127**, 217601 (2021).
- [25] M. H. Christensen, T. Biro, B. M. Andersen, and R. M. Fernandes, Loop currents in AV_3Sb_5 kagome metals: Multipolar and toroidal magnetic order, *Phys. Rev. B* **106**, 144504 (2022).
- [26] S.-Y. Yang, Y. Wang, B. R. Ortiz, D. Liu, J. Gayles, E. Derunova, R. Gonzalez-Hernandez, Sejkal, Y. Chen, S. S. P. Parkin, S. D. Wilson, E. S. Toberer, T. McQueen, and M. N. Ali, Giant, unconventional anomalous Hall effect in the metallic frustrated magnet candidate, KV_3Sb_5 , *Sci. Adv.* **6**, eabb6003 (2020).
- [27] F. H. Yu, T. Wu, Z. Y. Wang, B. Lei, W. Z. Zhuo, J. J. Ying, and X. H. Chen, Concurrence of anomalous Hall effect and charge density wave in a superconducting topological kagome metal, *Phys. Rev. B* **104**, L041103 (2021).
- [28] Y. Wang, Z. Chen, Y. Nie, Y. Zhang, Q. Niu, G. Zheng, X. Zhu, W. Ning, and M. Tian, Nontrivial Fermi surface topology and large anomalous Hall effect in the kagome superconductor RbV_3Sb_5 , *Phys. Rev. B* **108**, 035117 (2023).
- [29] C. Guo, C. Putzke, C. Konyzheva, S. Konyzheva, X. Huang, M. Gutierrez-Amigo, I. Errea, D. Chen, M. G. Vergniory, C. Felser, M. H. Fischer, T. Neupert, and P. J. W. Moll, Switchable chiral transport in charge-ordered kagome metal CsV_3Sb_5 , *Nature* **611**, 461 (2022).
- [30] Supplementary Information
- [31] R. Tazai, Y. Yamakawa, and H. Kontani, Charge-loop current order and Z_3 nematicity mediated by bond order fluctuations in kagome metals, *Nat. Commun.* **14**, 7845 (2023).
- [32] L. Yu, C. Wang, Y. Zhang, M. Sander, S. Ni, Z. Lu, S. Ma, Z. Wang, Z. Zhao, H. Chen, K. Jiang, Y. Zhang, H. Yang, F. Zhou, X. Dong, S. L. Johnson, M. J. Graf, J. Hu, H.-J. Gao, and Z. Zhao, Evidence of a hidden flux phase in the topological kagome metal CsV_3Sb_5 , arXiv:2107.10714 (available at <https://arxiv.org/abs/2107.10714>).
- [33] C. Mielke III, D. Das, J.-X. Yin, H. Liu, R. Gupta, Y.-X. Jiang, M. Medarde, X. Wu, H. C. Lei, J. Chang, P. Dai, Q. Si, H. Miao, R. Thomale, T. Neupert, Y. Shi, R. Khasanov, M. Z. Hasan, H. Luetkens, and Z. Guguchia, Time-reversal symmetry-breaking charge order in a kagome superconductor, *Nature* **602**, 245 (2022).
- [34] R. Khasanov, D. Das, R. Gupta, C. Mielke III, M. Elenker, Q. Yin, Z. Tu, C. Gong, H. Lei, E. T. Ritz, R. M. Fernandes, T. Birol, Z. Guguchia, and H. Luetkens, Time-reversal symmetry broken by charge order in CsV_3Sb_5 , *Phys. Rev. Res.* **4**, 023244 (2022).
- [35] Z. Guguchia, C. Mielke III, D. Das, R. Gupta, J.-X. Yin,

- H. Liu, Q. Yin, M. H. Christensen, Z. Tu, C. Gong, N. Shumiya, M. S. Hossain, T. Gamsakhurdashvili, M. Elander, P. Dai, A. Amato, Y. Shi, H. C. Lei, R. M. Fernandes, M. Z. Hasan, H. Luetkens, and R. Khasanov, Tunable unconventional kagome superconductivity in charge ordered RbV_3Sb_5 and KV_3Sb_5 , *Nat. Commun.* **14**, 153 (2023).
- [36] J. Luo, Z. Zhao, Y. Z. Zhou, J. Yang, A. F. Fang, H. T. Yang, H. J. Gao, R. Zhou, and G.-q. Zheng, Possible star-of-David pattern charge density wave with additional modulation in the kagome superconductor CsV_3Sb_5 , *npj Quantum Mater.* **7**, 30 (2022).
- [37] Y. Hu, S. Yamane, G. Mattoni, K. Yada, K. Obata, Y. Li, Y. Yao, Z. Wang, J. Wang, C. Farhang, J. Xia, Y. Maeno, and S. Yonezawa, Time-reversal symmetry breaking in charge density wave of CsV_3Sb_5 detected by polar Kerr effect, arXiv:2208.08036 (available at <https://arxiv.org/abs/2208.08036>).
- [38] C. Guo, G. Wagner, C. Putzke, D. Chen, K. Wang, L. Zhang, M. Gutierrez-Amigo, I. Errea, M. G. Vergniory, C. Felser, M. H. Fischer, T. Neupert, and P. J. W. Moll, Correlated order at the tipping point in the kagome metal CsV_3Sb_5 , *Nature Physics* **20**, 579 (2024).
- [39] R. Tazai, Y. Yamakawa, and H. Kontani, Drastic magnetic-field-induced chiral current order and emergent current-bond-field interplay in kagome metals, *Proc. Natl. Acad. Sci. (PNAS)* **121**, e2303476121 (2024).
- [40] K. Fujita, C. K. Kim, I. Lee, J. Lee, M. H. Hamidian, I. A. Firmo, S. Mukhopadhyay, H. Eisaki, S. Uchida, M. J. Lawler, E. -A. Kim, and J. C. Seamus Davis, Simultaneous transitions in cuprate momentum-space topology and electronic symmetry breaking, *Science* **344**, 612 (2014).
- [41] C. J. Butler, Y. Kohsaka, Y. Yamakawa, M. S. Bahramy, S. Onari, H. Kontani, T. Hanaguri, and S. Shamoto, Correlation-driven electronic nematicity in the Dirac semimetal BaNiS_2 , *Proc. Natl. Acad. Sci. USA*, **119**, e2212730119 (2022).
- [42] S. Wang, P. Choubey, Y. X. Chong, W. Chen, W. Ren, H. Eisaki, S. Uchida, P. J. Hirschfeld, and J. C. Seamus Davis, Scattering interference signature of a pair density wave state in the cuprate pseudogap phase, *Nat. Commun.* **12**, 6087 (2021).
- [43] F. Grandi, A. Consiglio, M. A. Sentef, R. Thomale, and D. M. Kennes, Theory of nematic charge orders in kagome metals, *Phys. Rev. B* **107**, 155131 (2023).
- [44] H. D. Scammell, J. Ingham, T. Li, and O. P. Sushkov, Chiral excitonic order from twofold van Hove singularities in kagome metals, *Nat. Commun.* **14**, 605 (2023).
- [45] K. Shimura, R. Tazai, Y. Yamakawa, S. Onari, and H. Kontani, Real-space loop current pattern in time-reversal-symmetry breaking phase in kagome metals, *J. Phys. Soc. Jpn.* **93**, 033704 (2024).
- [46] S. Onari, Y. Yamakawa, and H. Kontani, Sign-reversing orbital polarization in the nematic phase of FeSe due to the C_2 symmetry breaking in the self-energy, *Phys. Rev. Lett.* **116**, 227001 (2016).
- [47] R. Tazai, Y. Yamakawa, and H. Kontani, Emergence of charge loop current in the geometrically frustrated Hubbard model: A functional renormalization group study, *Phys. Rev. B* **103**, L161112 (2021).
- [48] R. Tazai, S. Matsubara, Y. Yamakawa, S. Onari, and H. Kontani, Rigorous formalism for unconventional symmetry breaking in Fermi liquid theory and its application to nematicity in FeSe , *Phys. Rev. B* **107**, 035137 (2023).
- [49] J. Huang, R. Tazai, Y. Yamakawa, S. Onari, and H. Kontani, Low temperature phase transitions inside the CDW phase in the kagome metals AV_3Sb_5 ($A=\text{Cs,Rb,K}$): Significance of mixed-type Fermi surface electron correlations, *Phys. Rev. B* **109**, L041110 (2024).
- [50] H. Kontani, R. Tazai, Y. Yamakawa, and S. Onari, *Unconventional density waves and superconductivities in Fe-based superconductors and other strongly correlated electron systems*, *Adv. Phys.* **70**, 355 (2021).
- [51] S. Nakazawa, R. Tazai, Y. Yamakawa, S. Onari, and H. Kontani, Giant Impurity Effects on Charge Loop Current Order States in Kagome Metals, *Phys. Rev. B* **111**, 075161 (2025).
- [52] H. Zhao *et al.*, Cascade of correlated electron states in the kagome superconductor CsV_3Sb_5 , *Nature* **599**, 216 (2021).
- [53] H. Li, H. Zhao, B. R. Ortiz, Y. Oey, Z. Wang, S. D. Wilson, and I. Zeljkovic, *Unidirectional coherent quasiparticles in the high-temperature rotational symmetry broken phase of AV_3Sb_5 kagome superconductors*, *Nat. Phys.* **19**, 637 (2023).
- [54] R. Tazai, Y. Yamakawa, T. Morimoto, and H. Kontani, Quantum-metric-induced giant and reversible nonreciprocal transport phenomena in chiral loop-current phases of kagome metals, arXiv:2408.04233.

[Supplementary Information]

Origin of switchable quasiparticle-interference chirality in loop-current phase of kagome metals measured by scanning-tunneling-microscopy

Seigo Nakazawa¹, Rina Tazai², Youichi Yamakawa¹, Seiichiro Onari¹, and Hiroshi Kontani¹¹ Department of Physics, Nagoya University, Nagoya 464-8602, Japan² Yukawa Institute for Theoretical Physics, Kyoto University, Kyoto 606-8502, Japan**A: Tight-binding model with BO and LC order parameters**

The bond/current order is the modulation of the hopping integral between i and j atoms due to the electron correlation, $\delta t_{ij}^{b/c}$. Theoretically, it is the symmetry breaking in the self-energy, and it is derived from the density-wave (DW) equation [1, 2]. The wavevectors of the bond and current orders correspond to the inter-sublattice nesting vectors \mathbf{q}_n ($n = 1 - 3$). The triple- Q ($3Q$) bond order between the nearest V atoms is given as

$$\delta t_{ij}^b = \phi_1 g_{ij}^{(1)} + \phi_2 g_{ij}^{(2)} + \phi_3 g_{ij}^{(3)}, \quad (\text{S1})$$

where $\phi \equiv (\phi_1, \phi_2, \phi_3)$ is the set of BO parameters with the wavevector \mathbf{q}_n , and $g_{ij}^{(n)} = g_{ji}^{(n)} = \pm 1$ for the nearest-neighbor sites (i, j) is the even-parity form factor for the BO. For $n = 1$, $g_{ij}^{(1)} = +1$ [-1] for sites (i, j) belongs to sublattices (1, 2), (4, 5), (8, 10), (11, 7) [(2, 4), (5, 1), (7, 8), (10, 11)]. Figure S1 (a) represents the $3Q$ bond order $\phi = \phi e_0$, where $e_0 = (1, 1, 1)/\sqrt{3}$. The TrH (SoD) bond-order is realized for $\phi > 0$ ($\phi < 0$). The enlarged unit cell contains twelve sublattices ($l = 1 \sim 12$). Sites A, B, and C in the main text respectively correspond to sites 10, 8, and 12.

Next, we explain the $3Q$ current order between the nearest V atoms. Its form factor with $\mathbf{q} = \mathbf{q}_1$, $f_{ij}^{(1)}$, is $+i$ for sites (i, j) belongs to sublattices (l, m) = (1, 2), (2, 4), (4, 5), (5, 1), and $-i$ for (7, 8), (8, 10), (10, 11), (11, 7). Odd parity relation $f_{ij}^{(1)} = -f_{ji}^{(1)}$ holds. Other form factors with \mathbf{q}_2 and \mathbf{q}_3 , $f_{ij}^{(2)}$ and $f_{ij}^{(3)}$, are also derived from Fig. S1 (b). Using $\mathbf{f}_{ij} = (f_{ij}^{(1)}, f_{ij}^{(2)}, f_{ij}^{(3)})$, the current order is

$$\delta t_{ij}^c = \eta_1 f_{ij}^{(1)} + \eta_2 f_{ij}^{(2)} + \eta_3 f_{ij}^{(3)}, \quad (\text{S2})$$

where $\boldsymbol{\eta} \equiv (\eta_1, \eta_2, \eta_3)$ is the set of current order parameters with the wavevector \mathbf{q}_n . Figure S1 (a) represents the $3Q$ current order $\boldsymbol{\eta} = \eta e_\alpha$, where $e_I = (a, -1, -1)/\sqrt{2+a^2}$, $e_{II} = (-1, a, -1)/\sqrt{2+a^2}$, and $e_{III} = (-1, -1, a)/\sqrt{2+a^2}$. When $|\eta/\phi| \ll 1$, the LC + BO coexisting state is given by $(\boldsymbol{\eta}_\alpha, \phi_0)$ with $a \lesssim 2$ according to the GL free-energy analysis. (For simplicity, we set $a = 2$ in this paper, although similar results are obtained for $a = 1$.) Then, the electronic states become nematic, with the director aligned the ab direction for $\alpha=I$,

the bc direction for $\alpha=II$, and the ca direction for $\alpha=III$. In the theoretical model of the main text, the tight-binding hopping integral is given as $t_{ij} = t_{ij}^0 + \delta t_{ij}^b + \delta t_{ij}^c$ [3, 4].

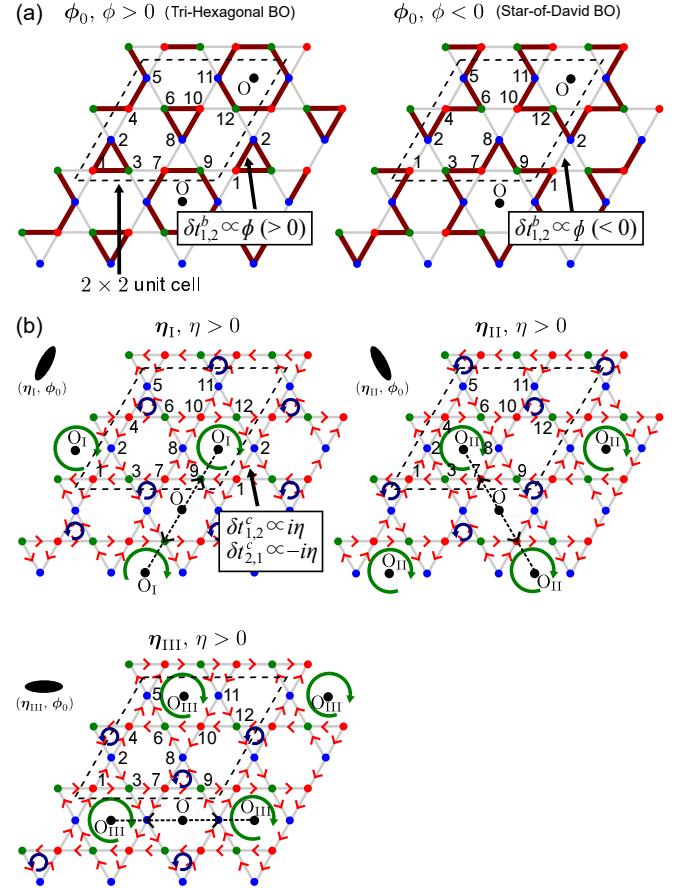


FIG. S1: (a) BO parameter ϕ_0 in real space for TrH pattern ($\phi > 0$) and SoD pattern ($\phi < 0$). (b) LC parameter η_α ($\alpha=I, II, III$) in real space ($\eta > 0$). Sites A, B, and C in the main text (in Fig. 1 (b) and Fig. 3 (c)) respectively correspond to sites 10, 8, and 12.

Figure S2 shows the modulation of the LDOS ($E = -0.04$) induced by a single Imp A in the absence of the LC order, for (a) no BO ($\phi = 0$) and (b) finite BO ($\phi = -0.01$). In both cases, the LDOS pattern exhibits mirror symmetry with respect to the mirror lines shown as dotted lines in Fig. S2. For this reason, impurity-induced QPI signal is achiral when the LC order is absent

($\eta = 0$).

In highly contrast, in the nematic LC + BO state, the LDOS pattern violates any mirror symmetries, as demonstrated in Fig. 2 (a) in the main text. For this reason, chiral QPI signal can be caused by dilute impurities. Notably, in the nematic LC + BO state, the chirality of this QPI signal can be flipped by applying small magnetic field B_z . This is the main finding of this paper.

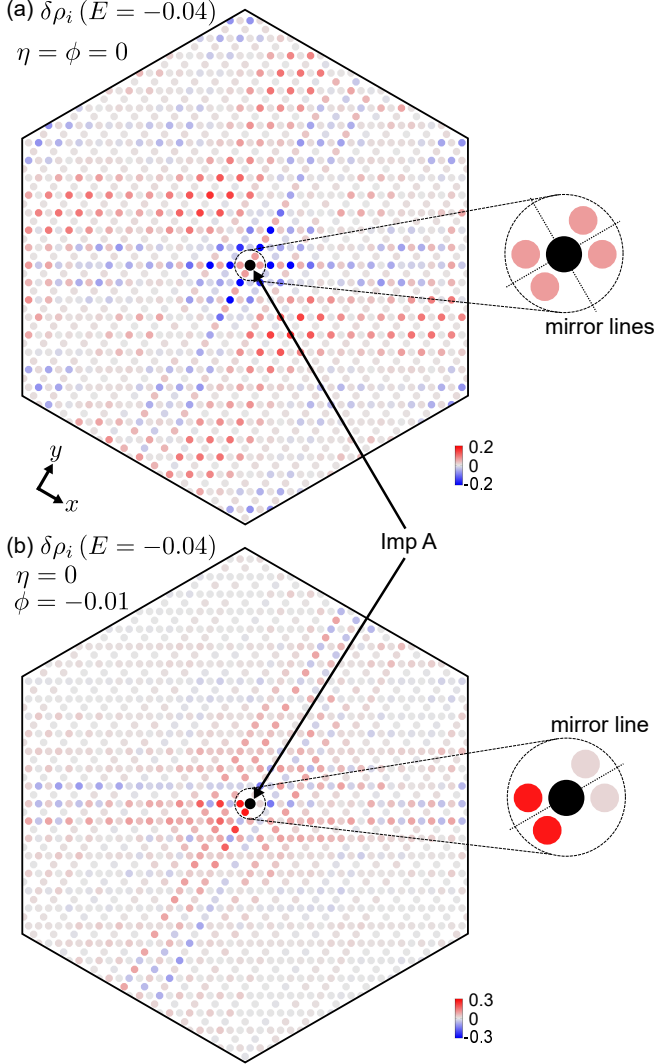


FIG. S2: Modulation of the LDOS ($E = -0.04$) induced by single Imp A in $N = 1452$ -site unit cell model in the absence of the LC order, for (a) no BO ($\phi = 0$) and (b) finite BO ($\phi = -0.01$). Both LDOS patterns are achiral and exhibit C_{1h} symmetry around Imp A.

B: GL free-energy for LC + BO state

To discuss the change in the QPI chirality by Imp Z ($\chi_Z = \pm 1, 0$) under small magnetic field, we analyze the GL free energy with respect to the LC and BO order pa-

rameters. The free-energy up to the fourth order terms is given as [2, 5] $F[\boldsymbol{\eta}, \boldsymbol{\phi}_0] = a_b|\boldsymbol{\phi}|^2 + a_c|\boldsymbol{\eta}|^2 + b_1\phi_1\phi_2\phi_3 + b_2(\phi_1\eta_2\eta_3 + \text{cycl.}) + c_1(\phi_1^4 + \phi_2^4 + \phi_3^4) + c_2(\phi_1^2\phi_2^2 + \text{cycl.}) + c_3(\eta_1^4 + \eta_2^4 + \eta_3^4) + c_4(\eta_1^2\eta_2^2 + \text{cycl.}) + 2c_5(\phi_1^2\eta_1^2 + \phi_2^2\eta_2^2 + \phi_3^2\eta_3^2) + c_6(\phi_1^2(\eta_2^2 + \eta_3^2) + \text{cycl.})$, where $a_b \propto (T_{\text{cdw}} - T)$ and $a_c \propto (T_{\text{lc}} - T)$ are the second-order, b_1 and b_2 are the third-order, and $c_1 \sim c_6$ are the fourth-order parameters. Here, we assume $\boldsymbol{\phi} = \phi_0$. Then, the ϕ^3 term becomes $b_1\phi^3/3\sqrt{3}$, so the relation $b_1\phi < 0$ is satisfied to stabilize the 3Q BO. Then, the GL free energy is simplified as $F[\boldsymbol{\eta}, \phi_0] = (a_c - b_1\phi/2\sqrt{3} + 2(c_1 + c_2)\phi^2/3)|\boldsymbol{\eta}|^2 + (-b_1\phi/2\sqrt{3})(\eta_1 + \eta_2 + \eta_3)^2 + c_1|\boldsymbol{\eta}|^4 + (c_2 - 2c_1)(\eta_1^2\eta_2^2 + \text{cycl.})$. Here, we used the approximate relation $b_2 = -b_1$, $c_1 = c_3 = c_5$, and $c_2 = c_4 = c_6$. Because $b_1\phi < 0$, the relation $\eta_1 + \eta_2 + \eta_3 = 0$ is satisfied for $|\boldsymbol{\phi}| \gg |\boldsymbol{\eta}|$. The 3Q (1Q) LC order is realized when $c_2 < 2c_1$ ($c_2 > 2c_1$). Thus, the stable 3Q LC + BO is $(\pm\boldsymbol{\eta}_\alpha, \phi_0)$, where $\alpha = \text{I, II, III}$. Experimentally, the 1Q LC is observed above T_{cdw} in Ref. [6], while it changes to the 3Q LC state in the CDW phase. Therefore, the relations $|c_1| \gg (c_2 - 2c_1)$ is expected to be realized. Based on the above considerations, the free-energy would be almost unchanged under the conditions (i) $\eta_1^2 + \eta_2^2 + \eta_3^2 \equiv \eta_0^2$ ($\eta_0 = \text{constant}$) and (ii) $\eta_1 + \eta_2 + \eta_3 = 0$. Thus, the free-energy is unchanged under the condition $\eta_0^2 = \eta_1^2 + \eta_2^2 + (\eta_1 + \eta_2)^2 = 2\eta_1^2 + 2\eta_2^2 + 2\eta_1\eta_2$.

Next, we introduce the GL expansion of the orbital magnetization. The orbital magnetization under the LC + BO state is $M_{\text{orb}} = m_1\boldsymbol{\phi} \cdot \boldsymbol{\eta} + m_2(\eta_1\phi_2\phi_3 + \text{cycl.}) + m_3\eta_1\eta_2\eta_3$ [7]. When $\boldsymbol{\phi} = \phi_0$, we obtain $M_{\text{orb}} = -m_3/3\sqrt{6}$ for $\boldsymbol{\eta} = +\boldsymbol{\eta}_\alpha$, and $M_{\text{orb}} = +m_3/3\sqrt{6}$ for $\boldsymbol{\eta} = -\boldsymbol{\eta}_\alpha$. Therefore, in the case of $m_3 < 0$, the state $\boldsymbol{\eta}_\alpha$ is realized under $B_z > 0$, and it is changed to $-\boldsymbol{\eta}_\alpha$ under $B_z < 0$.

C: QPI signals for Imp Z'' and Imp Z'''

In Fig. 2 (d) in the main text, we demonstrate the E -dependence of the QPI signals I_n ($n = 1, 2, 3$) in the presence of the single impurity site A (=Imp A). The same QPI signals are obtained for Imp A'. The locations of sites A, A' and other sites in the 12 unit cell are shown in Fig. 1 (b). Figure S3 (a) represents the QPI signals for Imp B. (The same results are obtained for Imp B'.) The obtained I_2 and I_3 are swapped with those in Fig. 2 (d) for Imp A. Figure S3 (b) represents the QPI signals for Imp C, where the relation $I_2 = I_3$ is exactly satisfied.

We also demonstrate the QPI signals for Imp A'' and Imp B'' in Figs. S3 (c) and (d), respectively. The locations of the sites A'' and B'' are shown in Fig. 1 (b). In these cases, the relation $I_2 \neq I_3$ is realized as anticipated from the symmetry argument. In addition, the obtained I_2 and I_3 for Imp A'' are swapped with those for Imp B''. However, the obtained I_2 and I_3 are very close, so it is difficult to observe the QPI chirality for Imp A'' and Imp B'' cases.

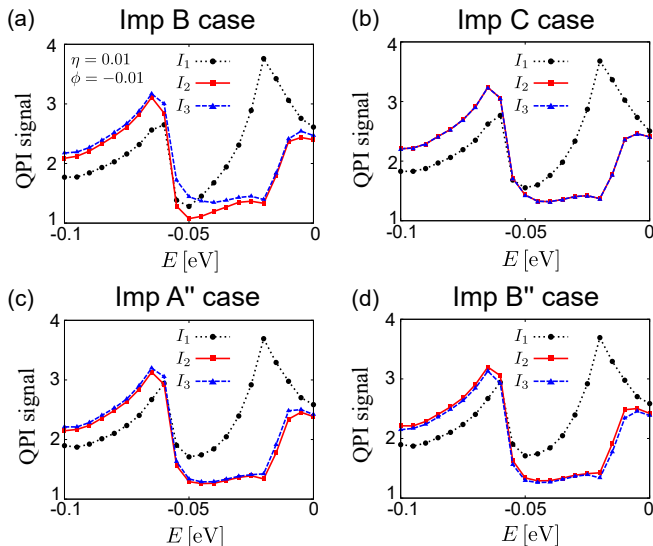


FIG. S3: Obtained QPI signals for (η_I, ϕ_0) : (a) In the case of Imp B, where the relation $I_2 \neq I_3$ is realized. Importantly, the obtained I_2 (I_3) is equivalent to I_3 (I_2) for Imp A, which is shown in the main text. (b) In the case of Imp C, where the relation $I_2 = I_3$ is realized. (c) In the case of Imp A'', where I_2 and I_3 are slightly different. (d) In the case of Imp B'', where I_2 (I_3) is equivalent to I_3 (I_2) for Imp A''.

D: Chiral QPI signal due to Sb-site impurities

In the main text, we discussed the QPI signal due to V-site impurity. Here, we perform the same study for Sb-site impurities (or vacancy), whose locations are depicted in Fig. S4 (a). They are above the V-atom kagome lattice plane. We introduce the potential of the nearest V-sites due to the impurity at Sb- n site, $V'(n_A + n_{B''} + n_C)$ for $n = 1$, $V'(n_{A''} + n_{B'} + n_C)$ for $n = 2$, and $V'(n_{A'} + n_{B'} + n_{C''})$ for $n = 3$, and so on. In the following numerical study, we set $V' = 1$.

Figure S4 (b) represents the obtained QPI signal due to Sb-1 site single impurity for $N = 1452$ ($M_x = M_y = 11$), for the LC + BO state (η_I, ϕ_0) with $\eta = -\phi = 0.01$. Thus, we obtain the prominent chiral QPI signal, originating from the violation of all 2D mirror symmetries due to the Sb-1 site impurity. The QPI chirality is reversed for Sb-2 site single impurity, as shown in Fig. S4 (c). In fact, the LDOS patterns with Sb-1 site impurity is converted to that with Sb-2 site through M_x operation. The same chirality is observed when a single impurity is introduced into Sb-1' and Sb-2', which are the inversions of Sb-1 and Sb-2, respectively. In contrast, when a single impurity is introduced at other Sb sites, the QPI signal becomes nematic.

To summarize, prominent chiral QPI signal can be driven by impurities on Sb-sites under the nematic LC + BO phase in kagome metals. The QPI chirality $\chi_{Z'} = \pm 1, 0$ depends on the Sb-site on the impurity denoted as Z' . Interestingly, the QPI signal exhibits sizable

chirality for wide range of E , compared with the V-site impurity case. Importantly, the QPI chirality due to a fixed Sb-site impurity $\chi_Z = \pm 1, 0$ is changed by reversing the magnetic field.

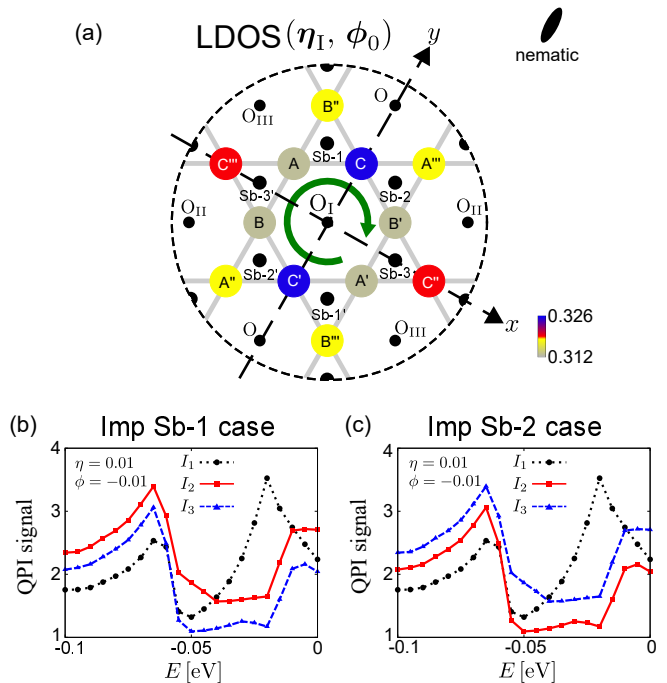


FIG. S4: (a) Positions of Sb-site above the V-atom kagome lattice. (b) Obtained chiral QPI signals for Sb-1 site impurity, (c) Sb-2 site impurity. Note that I_2 and I_3 in (b) are equal to I_3 and I_2 in (c), respectively.

E: Chiral QPI signal due to stripe CDW order in LC + BO phase

Figure S5 (a) represents the LC + BO phase (η_I, ϕ_0) , whose nematic director is along ab axis. Here, we also introduce the bc -direction stripe CDW with period $2a_0$. The yellow circles represent the stripe CDW potentials I_{st} , which is consistent with the energy-independent (vertical) QPI signal with period $2a_0$ is universally observed in CsV_3Sb_5 [8, 9]. In Fig. S5 (a), the stripe CDW is along the bc axis. When $I_{st} = 0$, the center of the hexagon with circulating current (indicated by the green arrow) is the center of inversion, and thus inversion symmetry exists. However, the inversion symmetry is broken for $I_{st} \neq 0$ [10]. For this reason, the giant nonreciprocal transport phenomenon under the magnetic field, called the electronic magneto-chiral anisotropy (eMChA), is realized in kagome metals [10, 11]. Figure S5 (b) represents the obtained QPI signals as functions of E , in the presence of the stripe CDW ($I_{st} = 0.01$) in the LC + BO phase. When $I_{st} = 0$, the relation $I_1 \neq I_2 = I_3$ is realized. However, I_2 and I_3 become inequivalent when $I_{st} \neq 0$.

Therefore, the chirality is induced by the stripe CDW, even in the absence of the impurity.

The nematic LC + BO state (η_I, ϕ_0) will be flipped to $(-\eta_{III}, \phi_0)$ or $(-\eta_{II}, \phi_0)$ [10]. The state $(-\eta_{III}, \phi_0)$ is schematically expressed in Fig. S5 (c). Figure S5 (d) shows the obtained QPI signal, where the signals I_1 and I_3 in Fig. S5 (b) are exchanged. (When $I_{st} = 0$, the relation $I_3 \neq I_1 = I_2$ is realized.) Importantly, the QPI chirality in Fig. S5 (b) and that in Fig. S5 (d) are opposite: For example, at $E = -0.1$, the relation $I_2 > I_3 > I_1$ holds in Fig. S5 (b), while the relation $I_2 > I_1 > I_3$ holds in Fig. S5 (d). The obtained results are consistent with the experimental report for A=Rb in Ref. [12].

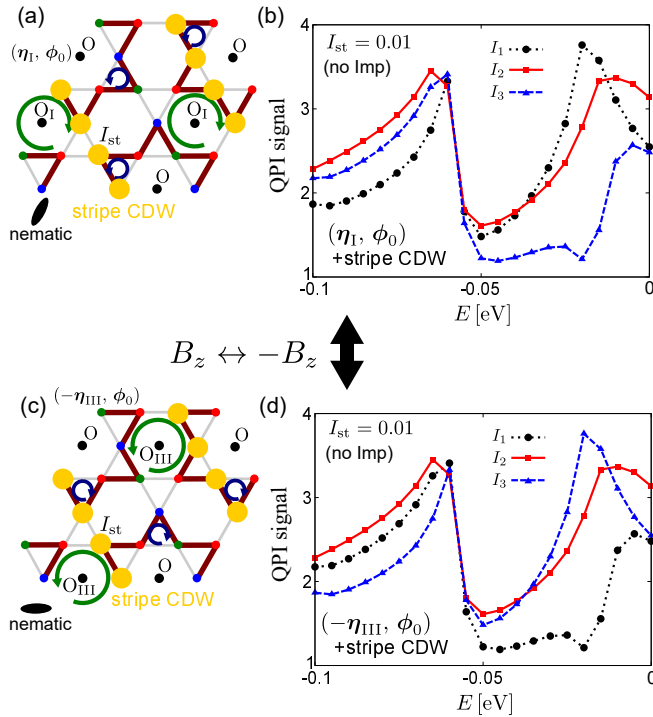


FIG. S5: (a) LC + BO phase (η_I, ϕ_0) with the $2a_0$ stripe CDW along ab direction, which is shown by the yellow circles. (b) Obtained chiral QPI signals in the presence of the stripe CDW ($I_{st} = 0.01$) in the LC + BO phase. The chirality is induced by the stripe CDW, even in the absence of the impurity. (c) LC + BO phase $(-\eta_{III}, \phi_0)$ with the $2a_0$ stripe CDW. (d) Obtained chiral QPI signals, whose chirality is opposite to the chirality in (b).

ventional superconductivity in kagome metal AV_3Sb_5 (A=K, Rb, Cs), *Sci. Adv.* **8**, eabl4108 (2022).

- [2] R. Tazai, Y. Yamakawa, and H. Kontani, Charge-loop current order and Z_3 nematicity mediated by bond order fluctuations in kagome metals, *Nat. Commun.* **14**, 7845 (2023).
- [3] K. Shimura, R. Tazai, Y. Yamakawa, S. Onari, and H. Kontani, Real-space loop current pattern in time-reversal-symmetry breaking phase in kagome metals, *J. Phys. Soc. Jpn.* **93**, 033704 (2024).
- [4] S. Nakazawa, R. Tazai, Y. Yamakawa, S. Onari, and H. Kontani, Giant Impurity Effects on Charge Loop Current Order States in Kagome Metals, arXiv:2405.12141.
- [5] T. Park, M. Ye, and L. Balents, Electronic instabilities of kagome metals: Saddle points and Landau theory, *Phys. Rev. B* **104**, 035142 (2021).
- [6] T. Asaba, A. Onishi, Y. Kageyama, T. Kiyosue, K. Ohtsuka, S. Suetsugu, Y. Kohsaka, T. Gaggli, Y. Kasahara, H. Murayama, K. Hashimoto, R. Tazai, H. Kontani, B. R. Ortiz, S. D. Wilson, Q. Li, H.-H. Wen, T. Shibauchi, and Y. Matsuda, Evidence for an odd-parity nematic phase above the charge-density-wave transition in a kagome metal, *Nat. Phys.* **20**, 40 (2024).
- [7] R. Tazai, Y. Yamakawa, and H. Kontani, Drastic magnetic-field-induced chiral current order and emergent current-bond-field interplay in kagome metals, *Proc. Natl. Acad. of Sci. (PNAS)* **121**, e2303476121 (2024).
- [8] H. Zhao *et al.*, Cascade of correlated electron states in the kagome superconductor CsV_3Sb_5 , *Nature* **599**, 216 (2021).
- [9] H. Li, H. Zhao, B. R. Ortiz, Y. Oey, Z. Wang, S. D. Wilson, and I. Zeljkovic, Unidirectional coherent quasiparticles in the high-temperature rotational symmetry broken phase of AV_3Sb_5 kagome superconductors, *Nat. Phys.* **19**, 637 (2023).
- [10] R. Tazai, Y. Yamakawa, T. Morimoto, and H. Kontani, Quantum-metric-induced giant and reversible nonreciprocal transport phenomena in chiral loop-current phases of kagome metals, arXiv:2408.04233.
- [11] C. Guo, C. Putzke, C. Konyzheva, S. Konyzheva, X. Huang, M. Gutierrez-Amigo, I. Errea, D. Chen, M. G. Vergniory, C. Felser, M. H. Fischer, T. Neupert, and P. J. W. Moll, Switchable chiral transport in charge-ordered kagome metal CsV_3Sb_5 , *Nature* **611**, 461 (2022).
- [12] Y. Xing, S. Bae, E. Ritz, Fan Yang, Turan Birol, Andrea N. Capa Salinas, Brenden R. Ortiz, Stephen D. Wilson, Z. Wang, R. M. Fernandes, and V. Madhavan, *Nature* **631**, 60 (2024).

[1] R. Tazai, Y. Yamakawa, S. Onari, and H. Kontani, Mechanism of exotic density-wave and beyond-Migdal uncon-